SUPPLEMENTARY MATERIAL

1. Catalogue of satellite images

The following section graphically presents the catalogue of optical and SAR satellite images utilised in this study. As illustrated in Figure S1, the optical satellite images include the designated study area, delineated within the reference coastal perimeter of Deception Island, including the BAEGC and BAD areas. Each image within light-blue the frame is identified by a label, as indicated in Table 2 of the main manuscript. The georeferencing of these images against the QB03 image was achieved through the application of a second-order polynomial transformation, utilising a set of control points, which were identified in each image as red cross-circle symbols. As indicated in each case by the total root mean square errors (RMSEs) resulting from the transformation carried out in ArcGIS Pro, the quality control measures are indicated for each image.

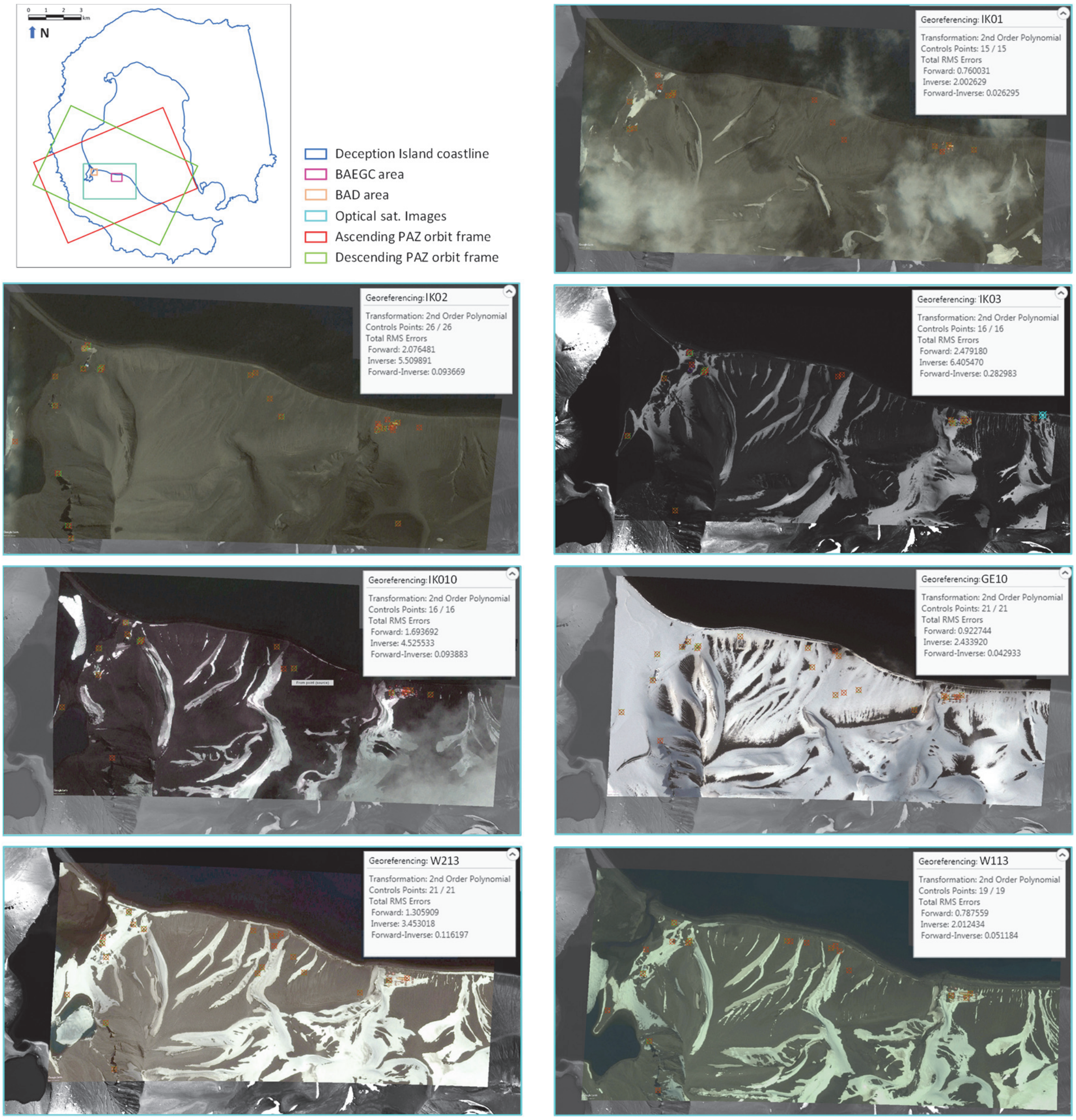

Figure S1. Geographical reference for the distribution of the satellite images used in this study. Optical satellite images georeferenced to QB03: IK01, IK02, IK03, IK10, GE10, W213 and W113, as listed in Table 2 of the main manuscript.

In Figure S2, the four original SAR-PAZ images used, were orthorectified using the SNAP software and the Range Doppler Terrain Correction (RDTC) algorithm, incorporating the REMA DEM, to produce the result here shown.

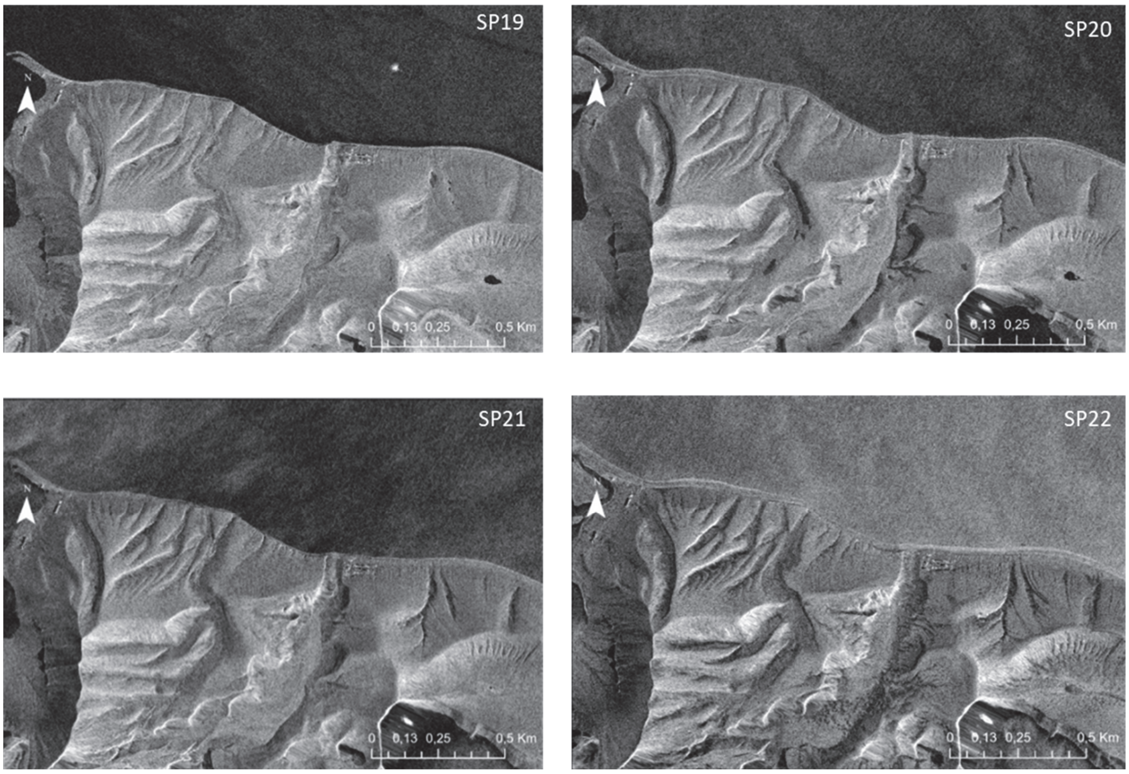

Figure S2. Orthorectified SAR satellite images. The labels identifying each image correspond to those listed in Table 2 of the main manuscript.

2. Weighting effect in the regression of least square models

This section summarises the effects observed in the results regarding instantaneous exchange rates, depending on the choice of weighting scheme applied in the least squares solution for the different regression models considered in this study: linear, quadratic and logistic.

Figure S3 shows the application of the linear model LM across the 294 transects distributed along the 16 digitised lines on each image of the studied bluff crest. The area of greatest uncertainty in the results is found in the central third (between 600 and 1100 m), with wider confidence intervals than in the other thirds. It can be seen that the pattern of behaviour of the EPR, R(t) = R constant, and the 95% and 99% confidence intervals is very similar regardless of the uncertainty weighting scheme applied to the data.

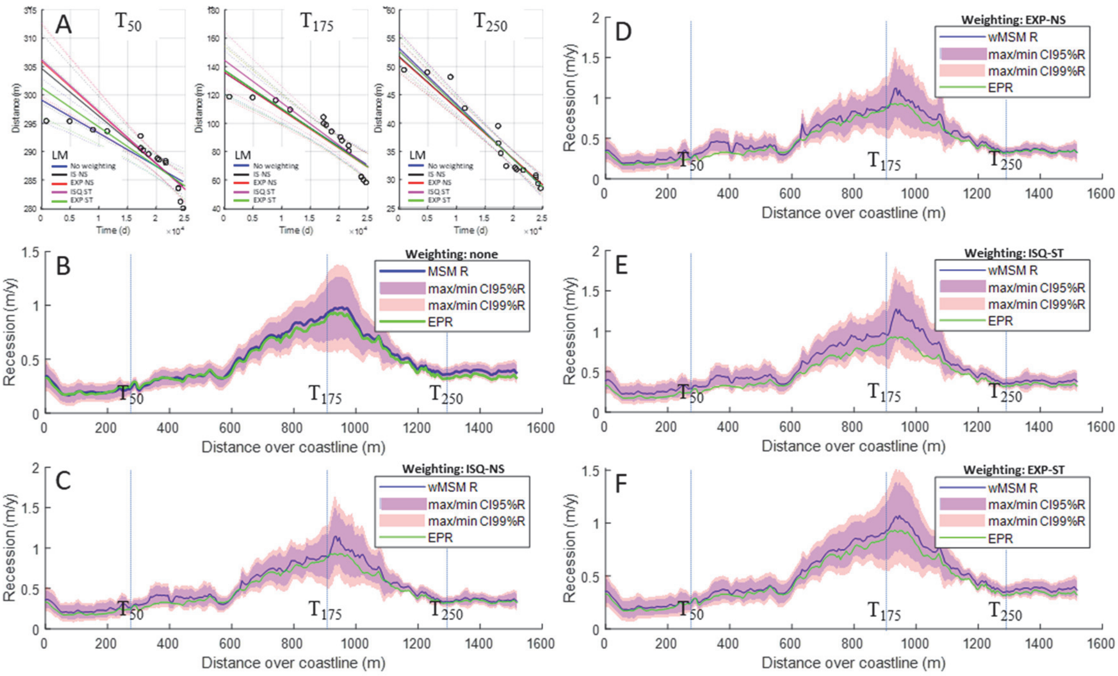

Figure S3. LM regression results: A) detail of the fitted LM to distance vs. time (days since FD56) at transects 50, 175 and 250 (solid lines) and their 95% prediction bounds across the LM fit range (dotted curves around each linear model), applying the four weighting schemes considered in this work and without weighting. Rate of change R (in m/y) fitted with the ML (blue line) by least squares method (MSM) with the confidence intervals (CI) on R (at 99% and 95%) and the end-point rate (EPR, plotted with green line) at each transect along the study area, in B) change rate result (MSM R) without weighting, in C) change rate result (wMSM R) with weighting (ISQ-NS), in D) change rate result (wMSM R) with weighting (EXP-NS), in E) change rate result (wMSM R) with weighting (ISQ-ST), and in F) change rate result (wMSM R) with weighting (EXP-ST). In each graph the location of the transects T50, T175, T250 used in A are marked.

Figure S4 shows the results of the instantaneous rate-of-change maps R(t) obtained using the quadratic model QM after solving the least-squares problem with and without data weighting. The maps are very similar regardless of the weighting scheme applied to the data.

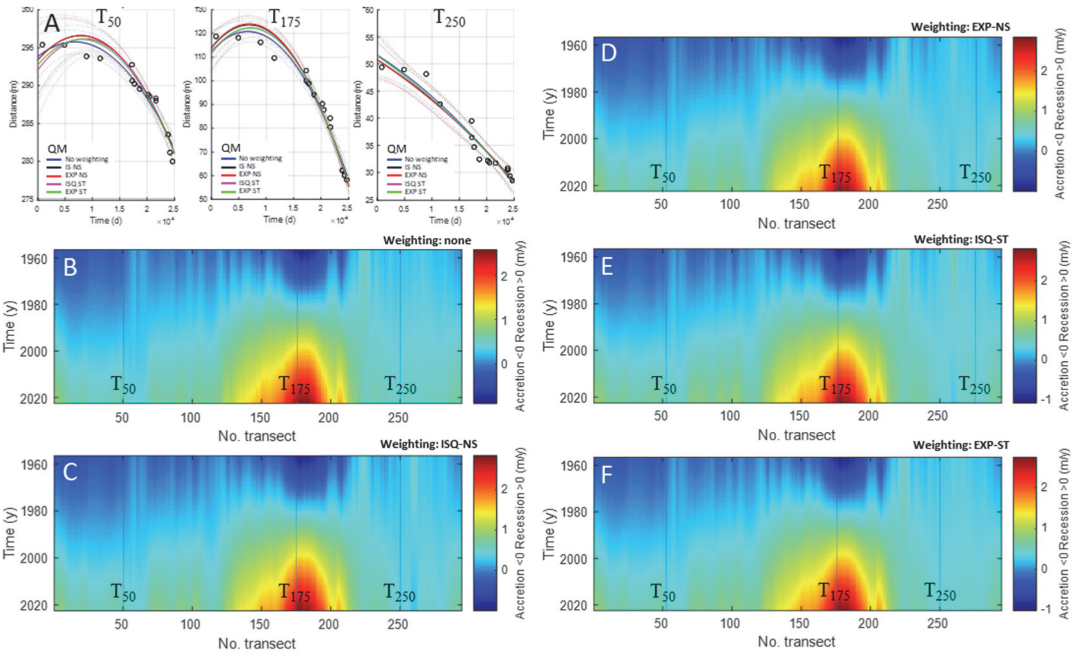

Figure S4. QM regression results: A) detail of the fitted LM to distance vs. time (days since FD56) at transects 50, 175 and 250 (solid parabolas) and their 95% prediction intervals across the QM fit range (dotted curves around each parabolic model), applying the four weighting schemes considered in this work and without weighting. Instantaneous rate of change R(t) map (in m/y) fitted with the QM along the time interval [1956, 2022] for each jth transect (j=1..294) along the study area, in B) R(t) map without weighting, in C) R(t) map with weighting (ISQ-NS), in D) R(t) map with weighting (EXP-NS), in E) R(t) map with weighting (ISQ-ST), and in F) R(t) map with weighting (EXP-ST). In each graph the location of the transects T50, T175, T250 used in A are marked.

Figure S5 shows the results of the instantaneous rate-of-change maps R(t) obtained using the three sigmoid models SL3, SL4 and SG4 after solving the least-squares problem with and without data weighting. For one model, the maps are more sensitive to the weighting scheme applied to the data.

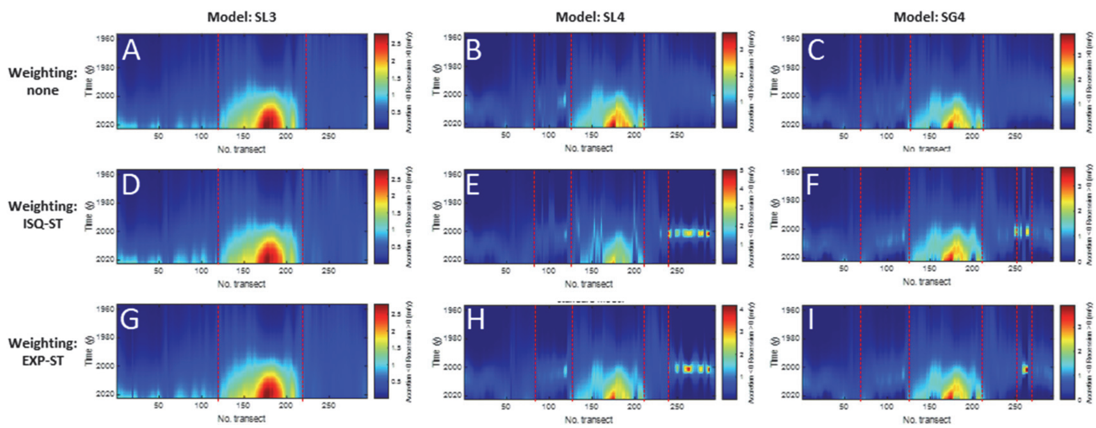

Figure S5. Instantaneous rate of change R(t) map (in m/y) fitted with the SL3, SL4 and SG4 (R(t) for each model in Table 5 of main manuscript) along the time interval [1956, 2022] for each jth transect (j=1..294) along the study area, first row R(t) maps (Figure S5 A to C) without weighting, second row R(t) maps (Figure S5 D to F) with weighting (ISQ-ST), and third row R(t) maps (Figure S5 G to I) with weighting (EXP-ST). The detected change in R(t) dynamics, along the study area, is marked with red dashed lines on each map.

3. **Influence of temporal sampling density.**

To assess the potential influence of temporal sampling density, a simple sensitivity test was performed by reducing the number of post-2000 observations to achieve a more homogeneous temporal distribution across the full time series.

To minimise the potential influence of temporal sampling bias, a temporally homogenised dataset was constructed by aggregating observations within fixed time windows (~10 years). For each interval, a representative shoreline position was obtained using the mean value of available data. This approach ensures a more uniform temporal distribution across the full period (1956–2022) and reduces the effect of uneven sampling density in recent decades.

A temporally homogenised dataset was constructed by selecting representative observations within successive time windows across the full period. We apply a time-window binning to the imaging dataset (Table S1). Within each window, if there are several data points, we select the one closest to the centre of the window in order to reduce noise, avoid arbitrary bias in the selection, and improve statistical robustness. For intervals with multiple observations (post-2000), a single representative value was selected based on its proximity to the centre of each time window, thereby reducing the influence of uneven sampling density.

Table S1. Time-window binning

Imaging source		Reference time (d)	Natural data grouping	Representative time (d)	Figure S6 data#
FIDASE 1956	FD56	20808	Low density	20808	1
SHNA 1968	SH68	24858		24858	2
BAS 1979	BA79	28920		28920	3
SAF 1986 west	SA86	31426	transition	31426	4
IKONOS2 2001	IK01	37232	Hight density	37271	5
IKONOS2 2002	IK02	37271			
IKONOS2 2003	IK03	37691		38645	6
QUICKBIRD 2005	QB05	38645			
IKONOS2 2010	IK10	40181		40467	7
GEOEYE1 2010	GE10	40467			
WORLDVIEW2 2013	W213	41612		41637	8
WORLDVIEW1 2013	W113	41637			
SAR PAZ 2019	SP19	43813		44209	9
SAR PAZ 2020	SP20	43835			
SAR PAZ 2021	SP21	44209			
SAR PAZ 2022	SP22	44653			

The sequence of the nine digitised lines along the crest of the bluff, which were analysed in this subsampling (Figure S6 A), produces a change envelope (Figure S6 B) with differences that are somewhat smaller than those in the complete original database, as certain elements have been removed (Table S1).

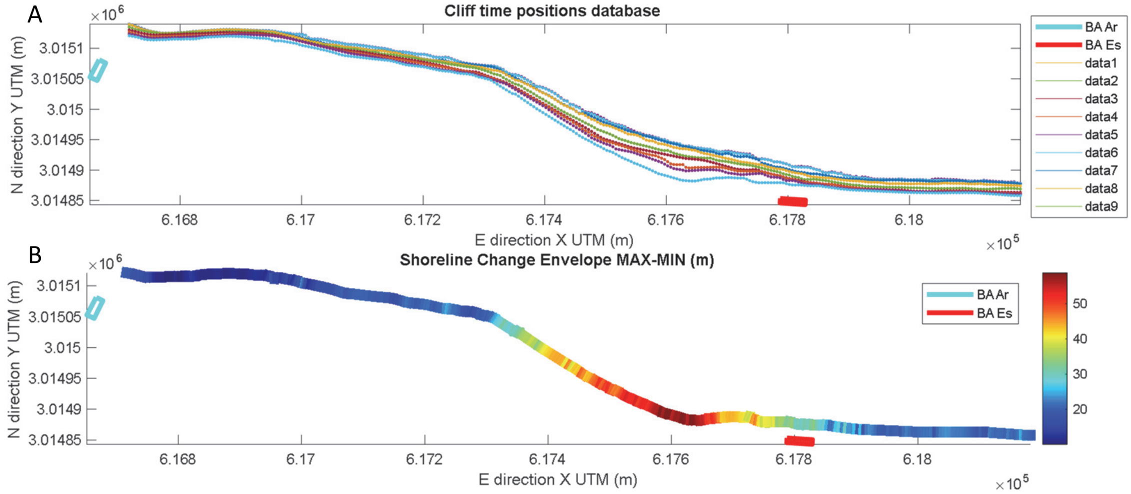

Figure S6. A) Catalogue of 9 polygonal lines extracted from the processing of the images in the study area and their discretisation into points with TBM (points on the polylines). B) Shoreline change envelope (SCE) between the first reference line (FIDASE 1956) and the last one (SAR PAZ 2021) in the temporally homogenised dataset.

To compare the results of the least-squares fit of the linear regression model (Figure 5 of the main manuscript), we present the results obtained both without weighting and using a standardised quadratic uncertainty weighting scheme (ISQ-ST). No major differences are observed along the coastline in the pattern of variation of the End Point Rate (EPR, green curve in Figure S7) or in the slope of the unweighted (MSM R) or weighted (wMSM R) regression line, for both the weighted and unweighted fits (blue curve in Figure S7). Similarly, the 95% and 99% confidence intervals (CI) (shown as pink and orange bands respectively in Figure S7) display ranges of uncertainty distributed across the study area from east to west, with no significant differences compared to those from the complete dataset comprising 16 cliff crest lines. The results are similar for other weightings considered in this study.

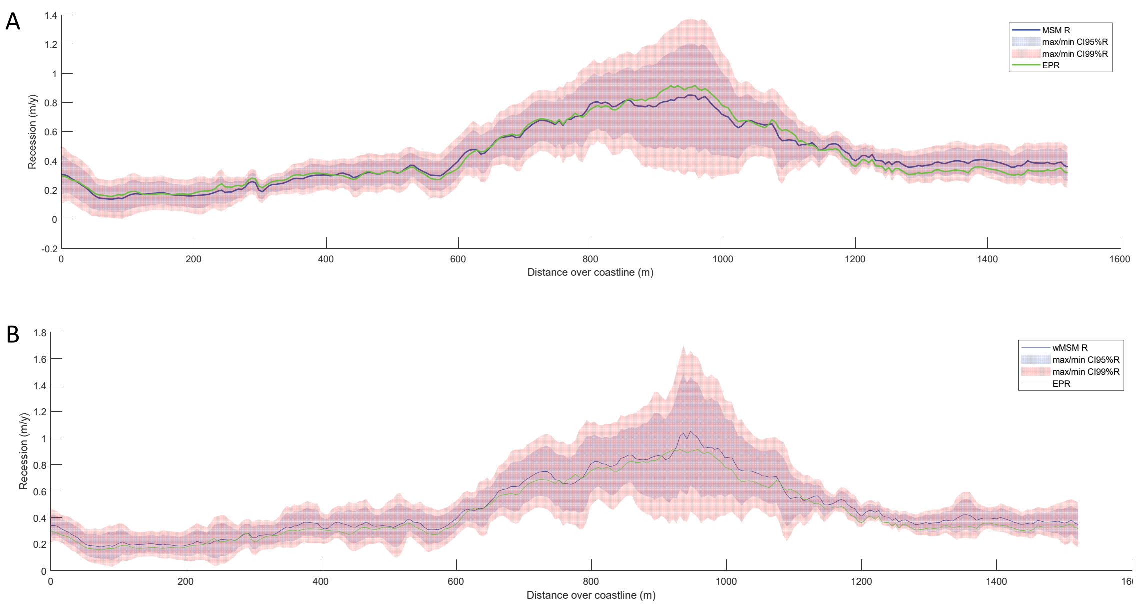

Figure S7. Recession R (in m/y) fitted with the ML (blue line) by least squares method (MSM) with the confidence intervals (CI) on R (at 99% and 95%) and the end-point rate (EPR, plotted with green line) at each transect along the study area, in A) recession result (MSM R) without weighting, in B) recession result (wMSM R) with weighting (ISQ-ST).

The results of the non-linear models analysed here to assess the possible influence of temporal sampling relate to the quadratic model QM and the Gompertz SG4 model, both ISQ-ST weighted (Figure S8). The remaining sigmoidal models (SL3 and SL4) behave in a similar manner to the Gompertz model. The quadratic model shows a spatiotemporal pattern (Figure S8 A) very similar to that described in the original manuscript (Figure 6 B to F), with rates of variation describing processes of weak accretion, in the area between transects 150 and 200 (mouth of the Mekong River) and in some other transects, which is not possible on the crest of a cliff. Furthermore, the maximum erosion rates fitted are somewhat higher than 2 m/year, as with the original dataset. Locally, a subtle difference is detected (around transect 210) as the slight increase in the erosion rate observed in the complete database in the present study is not detected. The SG4 model obtained from the homogenised reduced sample also exhibits a spatio-temporal pattern that is broadly similar to that of the original sample, with no anomalous rates of variation. As with the quadratic case, the details of temporal transitions such as those observed in the original data (Figure 6 in the main manuscript) are not clearly discernible.

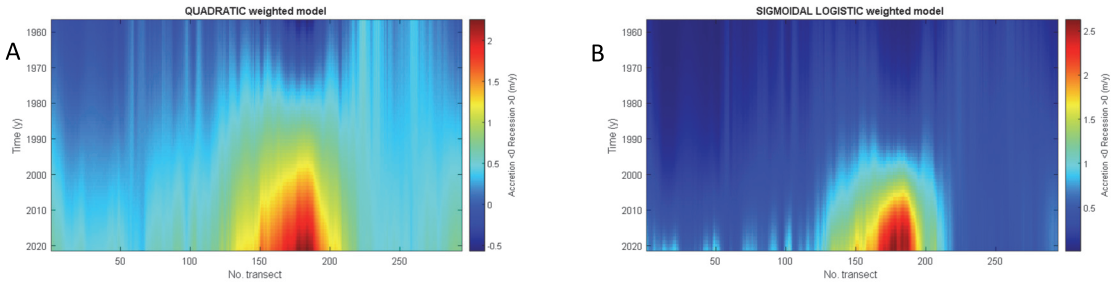

Figure S8. Instantaneous recession R(t) map (in m/y) fitted with the quadratic (A) and SG4 (B) models with the time homogenised dataset, for each j-th transect (j=1…294).

We can therefore state that the effect of the temporal homogenisation applied smooths out the temporal variations that had been identified as short-term local effects, but allows the overall pattern of behaviour to be maintained—a pattern more characteristic of the system itself than of an effect due to sampling density.

Locally across the transects, and particularly for the three used as examples in the original manuscript (T50, T175 and T250), the effect of temporal homogenisation of the database used does not result in any notable differences in the fit of the three models (linear, quadratic and Gompertz) employed here (Figure S9). The linear model, on each of the three transects, proves to be the poorest quality, with an RMSE of 0.6 m and an R^2 of 0.9 on T50 (280 m east of the origin), 2.7 m RMSE and 0.85 R^2 in T175 (at 900 m) and 0.5 RMSE and 0.95 R^2 in T250 (at 1300 m). The weighted quadratic model performs slightly better across all three transects, with an RMSE of 0.46 m and an R^2 of 0.95 at T50 (280 m east of the origin), an RMSE of 0.8 m and an R^2 of 0.98 at T175 (at 900 m) and 0.5 m RMSE and 0.97 R^2 at T250 (at 1300 m). Finally, the weighted SG4 model, across each of the three transects, proves to be the one with the best quality of the three compared here, in terms of its statistical metrics, with an RMSE of 0.44 m and an R^2 of 0.96 at T50 (280 m east of the origin), 0.5 m RMSE and 0.99 R^2 in T175 (at 900 m) and 0.5 m RMSE and 0.97 R^2 in T250 (at 1300 m). Furthermore, in terms of the validity of the result, as it does not show a range of unrealistic values (as the grid does) in the exchange rate.

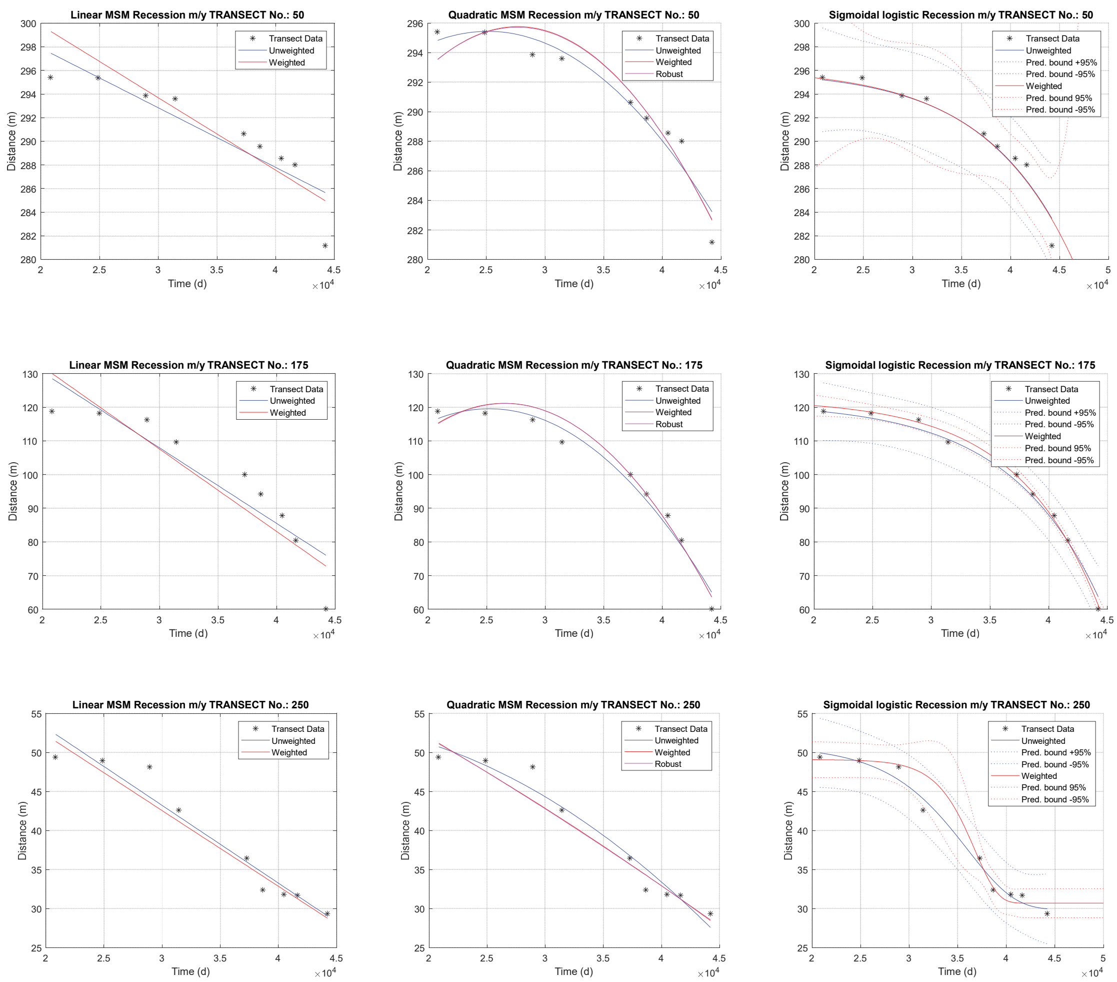

Figure S9. Regression results from LM, QM and SG4 models to distance vs. time at control transects T50, T175 and T250 (solid curves) using the time homogenised dataset.

Therefore, the sigmoidal behaviour and general pattern of accelerated retreat were preserved under this reduced dataset, although the precise timing of the inflexion point showed minor variations. This suggests that the identified non-linear trend is not solely an artefact of increased sampling density in post-2000 recent decades, but reflects a robust feature of the shoreline evolution.